npj | 2D materials and applications

www.nature.com/npj2dmaterials

ARTICLE OPEN

Nanomechanical probing and strain tuning of the Curie temperature in suspended $Cr_2Ge_2Te_6$-based heterostructures

Makars Šiškins[1]✉, Samer Kurdi[1], Martin Lee[1], Benjamin J. M. Slotboom[1], Wenyu Xing[2], Samuel Mañas-Valero[3], Eugenio Coronado[3], Shuang Jia[2], Wei Han[2], Toeno van der Sar[1]✉, Herre S. J. van der Zant[1]✉ and Peter G. Steeneken[1,4]✉

Two-dimensional magnetic materials with strong magnetostriction are attractive systems for realizing strain-tuning of the magnetization in spintronic and nanomagnetic devices. This requires an understanding of the magneto-mechanical coupling in these materials. In this work, we suspend thin $Cr_2Ge_2Te_6$ layers and their heterostructures, creating ferromagnetic nanomechanical membrane resonators. We probe their mechanical and magnetic properties as a function of temperature and strain by observing magneto-elastic signatures in the temperature-dependent resonance frequency near the Curie temperature, T_C. We compensate for the negative thermal expansion coefficient of $Cr_2Ge_2Te_6$ by fabricating heterostructures with thin layers of WSe_2 and antiferromagnetic $FePS_3$, which have positive thermal expansion coefficients. Thus we demonstrate the possibility of probing multiple magnetic phase transitions in a single heterostructure. Finally, we demonstrate a strain-induced enhancement of T_C in a suspended $Cr_2Ge_2Te_6$-based heterostructure by 2.5 ± 0.6 K by applying a strain of 0.026% via electrostatic force.

npj 2D Materials and Applications (2022)6:41 ; https://doi.org/10.1038/s41699-022-00315-7

The recent discovery of long range order in two-dimensional (2D) (anti)ferromagnets[1–3] has triggered extensive studies of 2D materials to experimentally probe magnetism of reduced dimensionality[4]. One material of particular interest is $Cr_2Ge_2Te_6$ (CGT)—a semiconducting ferromagnet with a bulk Curie temperature, T_C, ~ 60–66 K[2,5] with inter- and intra-layer ferromagnetic coupling for any number of layers[2]. Recent progress has been made in manipulating the magnetic order of CGT using electrostatic gating[6,7], magnetic field[2,8], pressure[9,10], ion intercalation[11], and via spin-orbit torque[12,13]. Mechanical strain offers another degree of freedom for such manipulation as bulk CGT was recently shown to exhibit strong spin-lattice coupling[9,14] and a negative thermal expansion coefficient near T_C[5], which is common amongst bulk chromium-based magnetic van der Waals crystals, like CrI_3, $CrCl_3$, $CrBr_3$ and $Cr_2Si_2Te_6$[15–18]. However, the coupling between magnetic order and strain in thin CGT has not been studied experimentally, as strain is a difficult parameter to control in substrate-supported ultrathin layers[19,20].

Emerging nanomechanical methods allow for high-precision strain manipulation and control when 2D materials are suspended forming ultrathin membrane resonators[21,22]. Due to the combination of low mass, high strength[23] and high frequency tunability[21,24], these membranes find potential use in a wide range of sensor applications[25] as well as in high-performance nanoelectromechanical systems, where these are used as probes for nonlinear dynamics and condensed matter effects in the materials they are made of[26]. The resonance frequency of these membranes can be tuned over a large range by strain[21], which can be controlled both statically[23] and dynamically[21,22]. Moreover, the difference between the thermal expansion coefficient of suspended 2D material layers and the substrate[27,28] or other materials in a heterostructure[29,30] provides additional routes for strain engineering, leading to either stretching or compressing ultrathin layers. Nanomechanical strain can also be used to probe magnetic states of membrane material[27] and switch between these states[30,31]. The relation between strain, a material's thermal expansion coefficient, and its magnetic properties result in the coupling between mechanical and magnetic degrees of freedom, which allows the investigation of magnetic phase transitions in 2D layered material membranes[27,30].

Here, we demonstrate that the magnetic phase transition of suspended thin CGT membranes can be probed mechanically via the temperature-dependent resonance frequency. CGT is known to exhibit high magnetostriction, i.e., a strong magneto-elastic coupling between magnetic order and the lattice[5,9,14], that deforms the crystal near T_C[5]. Thus, to control the strain in thin CGT flakes and deterministically probe the transition temperature, we choose other 2D material layers, WSe_2 and $FePS_3$, with positive thermal expansion coefficient and integrate them to form heterostructure membranes with CGT[29,32–34], which are important to compensate CGT's negative thermal expansion[5]. We then use these heterostructure membranes to probe and analyze the effect of the mutual interaction between the different 2D materials and CGT, and study the effect of electrostatically induced strain on the ferromagnetic order near T_C.

RESULTS

Mechanical properties of CGT membranes

The force-deflection curve of suspended membranes contains information about mechanical properties of the material. Thus, we first study thin layers of CGT by a static deflection method[23,35]. We fabricate a freestanding membrane by suspending a mechanically exfoliated thin CGT flake over a circular hole (Fig. 1a). We then apply the atomic force microscopy (AFM) force nanoindentation method[23,35] to indent the centre of the membrane with the tip of

[1]Kavli Institute of Nanoscience, Delft University of Technology, Lorentzweg 1, 2628 CJ Delft, The Netherlands. [2]International Center for Quantum Materials, Peking University, 5 Summer Palace Road, 100871 Beijing, China. [3]Instituto de Ciencia Molecular (ICMol), Universitat de València, c/Catedrático José Beltrán 2, 46980 Paterna, Spain. [4]Department of Precision and Microsystems Engineering, Delft University of Technology, Mekelweg 2, 2628 CD Delft, The Netherlands. ✉email: m.siskins-1@tudelft.nl; t.vandersar@tudelft.nl; h.s.j.vanderzant@tudelft.nl; p.g.steeneken@tudelft.nl

an AFM cantilever to cause a deflection of the membrane δ, as shown in Fig. 1b. The force applied to the centre of the membrane, F, is proportional to the stiffness k_c of the cantilever used and its deflection, Δz_c. Using cantilevers with calibrated stiffnesses, we record the force versus membrane deflection curves of this membrane, as depicted in Fig. 1c with filled blue circles. The observed trend can be described by the point-force deflection model for a circular membrane, assuming negligible tip radius compared to the membrane diameter[23,35]:

$$F = \left(\frac{4\pi E}{3(1-\nu^2)}\frac{h^3}{r^2}\right)\delta + (n_0\pi)\delta + \left(\frac{q^3 Eh}{r^2}\right)\delta^3, \quad (1)$$

where E is the Young's modulus of the membrane, r the membrane radius, h the membrane thickness, $\nu = 0.22$ the Poisson ratio of CGT[36], n_0 the pre-tension, and $q = 1/(1.05 - 0.15\nu - 0.16\nu^2)$ is a dimensionless geometrical parameter. To our knowledge, the Young's modulus of CGT has not been experimentally studied. We, therefore, extract its Young's modulus E_{CGT} from the experimental data using Eq. (1), as shown in Fig. 1c by the solid magenta line. To obtain a more reliable estimate of E_{CGT}, we measure 18 different membranes of varying thicknesses ($h = 9.5$–30.1 nm) and radii ($r = 1$–2.5 μm). We find a mean value, $E_{CGT} = 56.2 \pm 8.2$ GPa, as shown in the inset of Fig. 1c. The obtained value of E_{CGT} is consistent with the calculated[37] 2D Young's modulus of CGT, $E_{2D} = 41.8$ N m^{-1}, which yields to $E = E_{2D}/h_{2D} = 61.0$ GPa, in which h_{2D} is the single-layer thickness, taken as a third of that of the unit cell of CGT[5]: $h_{2D} = 2.056\,\text{nm}/3 \approx 0.685$ nm. The standard deviation for our measurements is comparable to that reported in similar experiments on other 2D material membranes[23,35]. We also found no layer number dependence for the studied range of thicknesses[38] (see Supplementary Note 1).

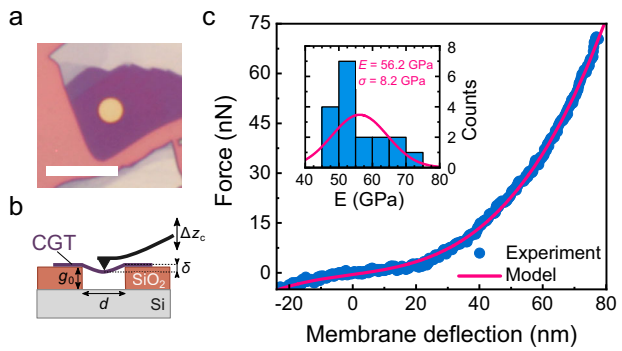

Fig. 1 Force indentation of suspended membranes of CGT. a An optical image of a 9.5 ± 0.3 nm thin CGT membrane with a radius $r = 2$ μm. Scale bar: 12 μm. **b** A schematic of the membrane deflection by a cantilever tip. Δz_c is the cantilever deflection, $g_0 = 285$ nm the separation between the membrane and the bottom Si substrate, d the membrane diameter, and δ the membrane deflection. **c** A force versus membrane deflection plot of the membrane shown in (**a**). Experimental data (filled blue circles) are fit by the point-force deflection of a circular membrane model of Eq. (1) (solid magenta line). The inset shows a histogram of the Young's moduli extracted from 18 CGT membranes of 9.5–30.1 nm thicknesses (see Supplementary Note 1), which were used to obtain the mean value of the Young's modulus E and corresponding standard deviation σ.

Resonating membranes

In order to study the coupling between the magnetic phase and the mechanical motion, we further investigate the dynamic nanomechanical properties of these membranes as a function of temperature. The temperature dependence of the mechanical resonances of the magnetic membranes is sensitive to changes in the magnetization of the 2D layers[30] and the magnetic phase, via a mechanism that couples the specific heat to the membrane tension via the thermal expansion coefficient[27]. Thus, by observing changes in motion of the membrane at T_C it is possible to probe the ferromagnetic to paramagnetic transition via the mechanical resonance frequency[27]. To do this, we use a laser interferometry technique[27,39] (Fig. 2a and "Methods"). A CGT membrane (see the inset of Fig. 2b) is placed in the chamber of an optical cryostation. We use a power-modulated blue laser to opto-thermally excite a fundamental resonance mode of the membrane, and a red laser to measure the change in the reflected signal due to the subsequent displacement of the membrane.

We first measure the resonance peak of the fundamental membrane mode at $T = 4$ K (blue circles in Fig. 2b). We fit the experimental data to a damped harmonic oscillator model (solid magenta line in Fig. 2b) to determine the frequency of the fundamental membrane mode, f_0. Subsequently, while recording $f_0(T)$ we heat the sample to $T = 78$ K, above the expected T_C of 66 K[2,5], and cool it down to $T = 4$ K. We plot the experimental data for the heating (filled blue circles) and the cooling (open blue circles) cycle in Fig. 2c. As the CGT membrane is cooled through the T_C, its resonance frequency f_0 reduces from 19.3 MHz at 78 K to 6.3 MHz at 4 K. To describe the $f_0(T)$ behaviour of CGT, we model the resonance frequency of a circular membrane as:

$$f_0(T) = \sqrt{\left(\frac{2.4048}{2\pi r}\right)^2 \frac{n_{th}(T)}{\rho h} + f_0^2(T_0)}, \quad (2)$$

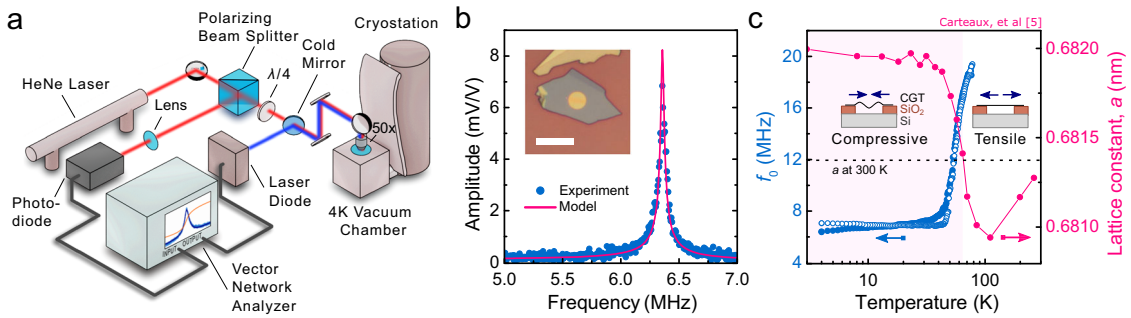

Fig. 2 CGT membrane characterization using laser interferometry. a Schematic diagram of the laser interferometry setup. **b** Filled blue circles—measured amplitude of the fundamental resonance peak at $T = 4$ K. Solid magenta line—fit to a damped harmonic oscillator model. The inset shows an optical image of a 17.4 ± 0.3 nm thin CGT membrane of 2 μm radius. Scale bar: 8 μm. **c** The comparison of the measured resonance frequency f_0 of the thin film shown in (**b**) (see also Supplementary Note 2) and the lattice constant of bulk CGT as a function of temperature. The filled and open blue circles represent the measured data during heating and cooling cycles respectively. The connected magenta circles represent the lattice constant a of bulk CGT as measured by Carteaux et al.[5]. The dashed black horizontal line represents a at $T = 300$ K. The insets show schematics of membrane stretching or buckling at tensile or compressive strain, on the right and left respectively. The pink region indicates the temperature range where compressive strain is dominant and is a guide to an eye.

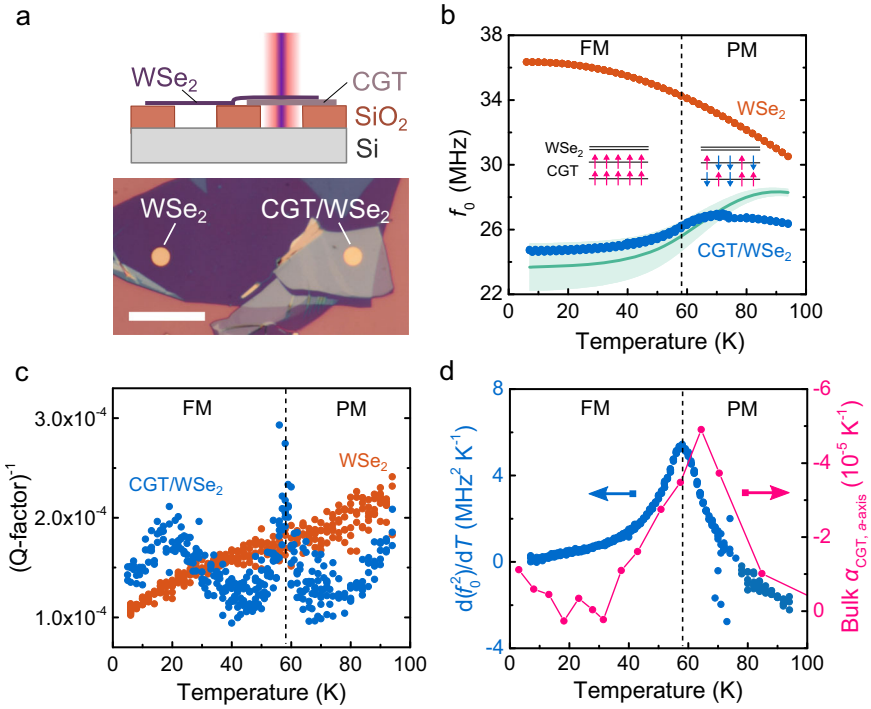

Fig. 3 Mechanical properties of a suspended CGT/WSe_2 (16.7 ± 0.3 nm/6.9 ± 0.1 nm) heterostructure membrane with a radius $r = 2$ µm. **a** Top panel: Schematic cross-section of the sample consisting of the suspended CGT/WSe_2 heterostructure membrane and the reference WSe_2 membrane of the same flake. Bottom panel: Optical image of the sample with specific membranes indicated. Scale bar: 16 µm. **b** Measured resonance frequencies f_0 of the membranes in (**a**). Solid green line—the fitted model of the resonance frequency of the CGT/WSe_2 heterostructure (Eq. (4)). Light green region—the allowed higher and lower boundary of the model due to the uncertainties in $h_{1,2}$, $E_{1,2}$ and $f_0^2(T_0)$. Insets: Schematic of a CGT/WSe_2 structure with the collinear and random magnetic spin arrangement in a bilayer of CGT in the ferromagnetic (FM) and the paramagnetic (PM) phases respectively. **c** Dissipation factor Q^{-1} as a function temperature. The origin of a broad feature at ~20 K remains unclear and is a subject of future studies. **d** Filled blue circles—$\frac{d(f_0^2)}{dT}$ of the CGT/WSe_2 heterostructure as a function of temperature. Connected magenta circles—the thermal expansion coefficient of bulk CGT[5]. The black vertical dashed lines in (**b**–**d**) indicate the measured $T_C^* = 58 \pm 0.5$ K as determined from the peak position of $\frac{d(f_0^2)}{dT}$.

where $f_0(T_0)$ is the resonance frequency at a reference temperature T_0 (e.g., room temperature) due to the contribution of the pre-tension and the bending rigidity, ρ the mass density, $n_{th}(T) = \frac{Eh}{(1-\nu)}\epsilon_{th}$ the thermally accumulated tension, $\epsilon_{th} = -\int_{T_0}^{T_i}(\alpha_{CGT}(T) - \alpha_{Si}(T))\,dT$ the thermal strain at an arbitrary temperature T_i[27,28], $\alpha_{Si}(T)$ the literature values for thermal expansion coefficient of Si substrate[40], and $\alpha_{CGT}(T)$ the temperature-dependent thermal expansion coefficient of CGT. Thus, we attribute the observed $f_0(T)$ trend to a large change in the in-plane lattice constants of the unit cell and the resulting negative $\alpha_{CGT}(T)$ near the phase transition, which was also previously reported for bulk CGT[5]. This anomalous lattice expansion, when cooling down from the paramagnetic to the ferromagnetic state, is related to the strong magnetostriction effect at the ferromagnetic ordering temperature T_C in CGT[5,14] that causes a substantial drop in strain $\epsilon_{th}(T)$ and a corresponding reduction of the membrane tension near T_C.

In Fig. 2c we also plot the change of the in-plane lattice constant, a, of bulk CGT, experimentally obtained by Carteaux et al.[5], as a function of temperature and compare it with the observed resonance frequency. The lattice constant a is shown to be smaller at room temperature (indicated by the black horizontal dashed line) in comparison to temperatures below the paramagnetic to ferromagnetic phase transition (~66 K). Since the lattice constant increases, the suspended part of the flake effectively has a larger volume at $T < T_C$ than at room temperature, indicating a switch from tensile to compressive strain, as indicated by the pink region in Fig. 2c. In this temperature range, the compressively strained suspended flake is likely to sag, wrinkle, or buckle, which possibly explains a different warming and cooling trend for the resonance frequency $f_0(T)$. Buckling of thicker magnetic CGT layers itself is interesting for the future development of reprogrammable mechanical memory devices at nano- and micro-scale[41], utilizing the bi-stable states of a buckled thick flake[42,43]. However, in the case of thin membranes, due to the changing resonance mode shape in the compressive strain regime and the potential wrinkling, a comprehensive analysis of $f_0(T)$ using Eq. (2)[27] is not reliable for $T < T_C$ and thus cannot be applied directly to resonators made of bare CGT.

Tensile strain in heterostructure membranes

To prevent the compressive strain that can lead to wrinkling in CGT membranes, and controllably probe $f_0(T)$ near and below its phase transition temperature, we fabricate a suspended membrane heterostructure composed of CGT and WSe_2 flakes, shown in Fig. 3. WSe_2 is a material with well-known mechanical properties[28,44,45] that does not undergo a phase transition from 4 to 300 K[45]. In the heterostructure, its positive thermal expansion coefficient $\alpha_{WSe_2}(T)$ counteracts the negative $\alpha_{CGT}(T)$ near T_C of CGT, such that the total membrane stress remains tensile and f_0 can be used to probe $a(T)$ even below T_C.

We measure $f_0(T)$ of the suspended CGT/WSe_2 heterostructure together with a reference drum of the same WSe_2 flake (Fig. 3b). The $f_{0,WSe_2}(T)$ follows a monotonous increase trend with decreasing temperature (filled orange circles), as expected from its positive $\alpha_{WSe_2}(T)$[28,45]. In contrast, $f_{0,CGT/WSe_2}(T)$ has a downturn with decreasing temperature near the transition temperature

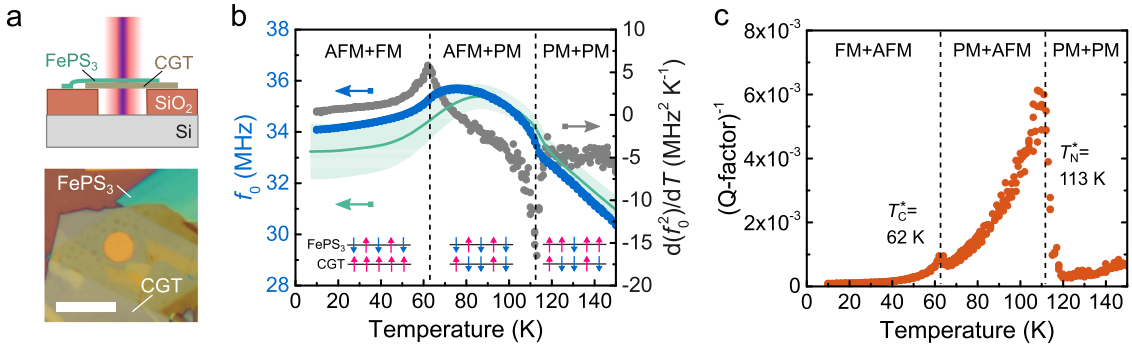

Fig. 4 Mechanical properties of a CGT/$FePS_3$ (19.8 ± 0.2 nm/18.0 ± 0.1 nm) heterostructure membrane with a radius $r = 2.5$ μm. a Top panel: A schematic cross-section of the suspended heterostructure membrane. Bottom panel: The optical image of the sample with the CGT/$FePS_3$ heterostructure. Scale bar: 10 μm. **b** Filled blue circles—the measured resonance frequency as a function of temperature. Filled grey circles—the temperature derivative of f_0^2. Solid green line—the heterostructure resonance frequency model as described by Eq. (4). The light green region indicates the higher and lower boundary of the model allowed due to the uncertainties in $h_{1,2}$, E_{CGT} and $f_0^2(T_0)$. The insets: Schematic pictures of a magnetic spin configuration in $FePS_3$ and CGT layers in corresponding combinations of antiferromagnetic (AFM), ferromagnetic (FM), and paramagnetic (PM) phases. **c** The dissipation factor Q^{-1} as a function temperature, in which the filled orange circles represent the measured data of the CGT/$FePS_3$ heterostructure. The black vertical dashed lines in (**b**) and (**c**) represent the measured $T_C^* = 62 \pm 1$ K of CGT and $T_N^* = 113 \pm 1$ K of $FePS_3$ as determined from positions of extrema in $\frac{d(f_0^2)}{dT}$ in (**b**).

(filled blue circles). This behaviour is distinct from the bare CGT resonator (Fig. 2c) due to the positive thermal expansion coefficient of the WSe_2 layer, which maintains a tensile total strain of the heterostructure and produces corresponding smaller tuning range of $f_{0,CGT/WSe_2}(T)$ near T_C.

We also plot the mechanical dissipation, the inverse of a quality factor $Q^{-1}(T)$, of both the WSe_2 and CGT/WSe_2 resonators in Fig. 3c. A notable peak in $Q_{CGT/WSe_2}(T)$ is visible at $T = 58$ K. We attribute this observation to an increase of the thermoelastic damping[46,47] expected near T_C in magnetic resonators[27]. This observation is supported by the measured maximum in $\frac{d(f_0^2)}{dT}$ (filled blue circles)[27] at 58 ± 0.5 K, the temperature which we define as T_C^* and indicated by the black vertical dashed lines in Fig. 3d. The observed maximum at T_C^* relates to the peak in the thermal expansion coefficient of CGT at T_C (filled magenta circles) that is shifted to lower temperatures in comparison to its bulk values of 60–66 K[2,5].

We model the resonance frequency of a heterostructure $f_{0,h}(T)$ by modifying Eq. (2) to describe the observations in Fig. 3b. We describe the total thermally accumulated tension of the CGT/WSe_2 heterostructure as a sum of individual tensions in each layer[29,33]:

$$\begin{aligned} n_{th}(T) &= n_{th,1}(T) + n_{th,2}(T) \\ &= \frac{E_1 h_1}{(1-\nu_1)}\epsilon_{th,1}(T) + \frac{E_2 h_2}{(1-\nu_2)}\epsilon_{th,2}(T). \end{aligned} \quad (3)$$

We assume that the slippage between the layers is negligible. Therefore, we obtain the final equation for the resonance frequency of the heterostructure as:

$$f_{0,h}(T) = \sqrt{\left(\frac{2.4048}{2\pi r}\right)^2 \frac{1}{\rho_1 h_1 + \rho_2 h_2} n_{th}(T) + f_0^2(T_0)}, \quad (4)$$

where n_{th} is given by Eq. (3). We plot the model of Eq. (4) for the CGT/WSe_2 heterostructure in Fig. 3b (solid green line). In doing so, we use the bulk $a_{CGT}(T)$ values[5], $\rho_{CGT} = 6091$ kg m^{-3} [5], $\nu_{CGT} = 0.22$[36], and $E_{CGT} = 56.2 \pm 8.2$ GPa for CGT; $\epsilon_{th,WSe_2}(T)$ extracted from the measured $f_{0,WSe_2}(T)$ of the reference drum using equation (2), $\rho_{WSe_2} = 9320$ kg m^{-3} [44,48], $\nu_{WSe_2} = 0.19$[44,49] and $E_{WSe_2} = 167.1 \pm 0.7$ GPa (measured for this membrane using the nanoindentation method described above, which is consistent which previous studies[44]) for WSe_2; and $f_0(94\text{ K}) = 27.2 \pm 0.4$ MHz. The resulting model reproduces the experiment qualitatively, yet lacks quantitative agreement above T_C, most likely due to the overestimation of $a_{CGT}(T)$ for thin layers of CGT in contrast to its bulk value[5].

Magnetic heterostructures

The presented methodology is not limited exclusively to the use of WSe_2, given that the thermal expansion coefficient of the added material is large and positive. To explore the possibility of detecting two magnetic phase transitions in the same membrane and also the possibility of having emergent properties arising from a coupling between the two flakes, we fabricate a heterostructure membrane made of a ferromagnetic CGT covered by an antiferromagnetic $FePS_3$ layer, which exhibits positive $a_{FePS_3}(T)$[27], as shown in Fig. 4a. Using the methods described above, we measure the resonance frequency of this suspended structure as a function of temperature. In Fig. 4b, we plot experimental $f_0(T)$ (filled blue circles) together with its $\frac{d(f_0^2(T))}{dT}$ (filled grey circles). The temperature derivative of f_0^2 shows two clear extrema, indicated by black vertical dashed lines: the first one at $T_C^* = 62 \pm 1$ K we attribute to the T_C of CGT[2,5]; the second one at $T_N^* = 113 \pm 1$ K corresponds to the Néel temperature, T_N, of $FePS_3$[3,27]. The temperatures at which these peaks appear correspond to the peaks in the specific heat of CGT and $FePS_3$, as a consequence of its relation to the thermal expansion coefficient $a(T)$[27,50].

We now analyze the measured $f_0(T)$ curve by plotting the model of Eq. (4) in Fig. 4b (solid green line) for the CGT/$FePS_3$ heterostructure using material parameters, such as $a(T)$, of CGT and $FePS_3$ obtained from literature[5,27,36] and E_{CGT} as determined from Fig. 1. We use $E_{FePS_3} = 103$ GPa, $\rho_{FePS_3} = 3375$ kg m^{-3}, $\nu_{FePS_3} = 0.304$[27,51] for $FePS_3$, and $f_0(150\text{ K}) = 30.9 \pm 0.7$ MHz. The model describes the experiment well with some deviations at low temperatures similar to the ones described above in Fig. 3c. In addition, we observe two peaks in $Q^{-1}(T)$, displayed in Fig. 4c, that we attribute to an increased thermoelastic damping near the phase transition[27,46,47]. The temperatures of these peaks coincide with the extrema from Fig. 4b, confirming the phase transitions in CGT and $FePS_3$.

Electrostatic strain tuning of T_C

Since strong magnetostriction is responsible for the large anomalies in the mechanical response of CGT membranes at T_C[5,14] (Fig. 1), we expect that the inverse effect should also be present allowing us to tune the T_C via strain[27,30]. To study this effect, we fabricate another CGT/WSe_2 heterostructure membrane contacted to Pd electrodes, as shown in Fig. 5a–c. We apply a gate

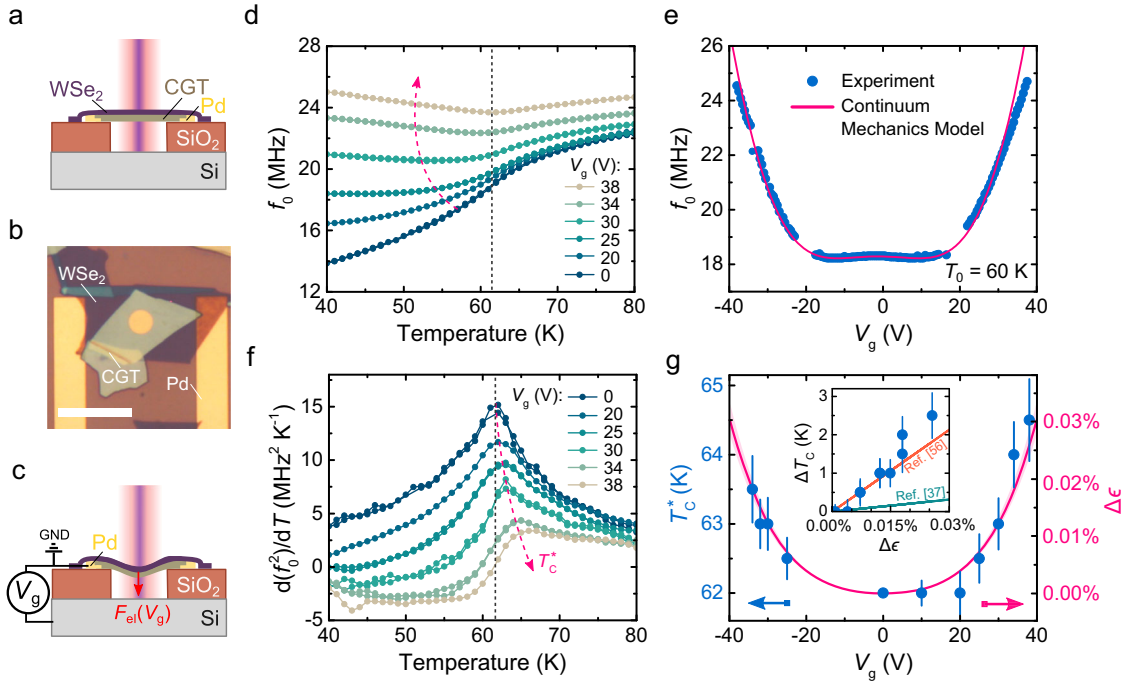

Fig. 5 Curie temperature enhancement as a function of strain in a suspended CGT/WSe_2 heterostructure (19.7 ± 0.1 nm/8.5 ± 0.2 nm). **a** The schematic cross-section of the suspended CGT/WSe_2 heterostructure membrane. **b** The optical image of the heterostructure with materials indicated. Membrane radius: $r = 2$ μm. Scale bar: 12 μm. **c** The schematics of the electrostatic strain-tuning principle. **d** Measured resonance frequencies f_0 of the heterostructure membrane as a function of temperature for different gate voltages V_g. **e** Filled blue circles—the measured resonance frequency as a function of V_g at 60 K. Solid magenta line—the continuum mechanics model fit[52,53]. **f** The temperature derivative of f_0^2 as a function of temperature for different V_g. The black vertical dashed lines in (**d**) and (**e**) show the peak position in $\frac{d(f_0^2)}{dT}$ at $V_g = 0$ V. **g** Filled blue circles—the shift in measured T_C^* as a function of V_g extracted from the peak position in (e). Solid magenta line—the estimate of electrostatically induced strain $\Delta\epsilon$ as a function of V_g (see Supplementary Note 3). The shaded magenta region shows the uncertainty in $\Delta\epsilon$. The inset shows $\Delta T_C = T_C^*(V_g) - T_C^*(0\,V)$ as a function of added voltage induced strain $\Delta\epsilon$ in addition to calculations from Li and Yang[37] (solid green line) and from Dong et al.[56] (solid orange line). The vertical error bars in T_C^* were estimated from determining the peak position in (**e**) within 2% accuracy in the measured maximum.

voltage V_g between the heterostructure membrane and the bottom Si substrate electrode to induce an electrostatic force, F_{el}, that pulls the membrane down and thus strains the CGT/WSe_2 stack. In Fig. 5d, we show the measured f_0 of the heterostructure membrane as a function of temperature for six different values of V_g. A notable increase of f_0 as a function of V_g is evident which is attributed to the electrostatic strain introduced. To describe the gate dependence of the resonance frequency, we show the $f_0(V_g)$ relationship near the phase transition temperature at $T_0 = 60$ K in Fig. 5e. We fit the measurement data to a continuum mechanics model of a circular membrane resonator[52,53] (see "Methods"), which describes the experiment well. We thus estimate the electrostatically added strain in CGT layer as:

$$\begin{aligned}\Delta\epsilon &= \epsilon_{el}(V_g) + \epsilon_b(V_g)\\ &\approx \left[\frac{2}{3}\left(\frac{\varepsilon_0 r}{8g_0^2 n(T_0)}\right)^2\right] V_g^4 + \left[\frac{\varepsilon_0 \Delta z(1-\nu)}{4g_0^2 n(T_0)}\right] V_g^2,\end{aligned} \quad (5)$$

where ϵ_{el} is the strain due to electrostatic pulling[30,53], ϵ_b the strain due to bending[54,55], $\Delta z = z_{neut} - z_{CGT}$ the distance from the neutral plane of the heterostructure z_{neut} to the central axis of CGT layer z_{CGT} (see Supplementary Note 3), ε_0 the dielectric permittivity of vacuum, and $n(T_0) = 2.538 \pm 0.003$ N m^{-1} the total tension in the suspended heterostructure at $T_0 = 60$ K (extracted from the fit in Fig. 5e).

Apart from the effect of electrostatically induced strain on $f_0(V_g)$ in Fig. 5d, the characteristic feature in the $f_0(T)$ curve, that we attribute to the Curie temperature of CGT[27], shifts to higher temperatures. This trend becomes even more apparent in Fig. 5f, where we plot $\frac{d(f_0^2)}{dT}$ for six different V_g. We extract T_C^* from the peak positions in $\frac{d(f_0^2)}{dT}$ for multiple V_g and plot it against the gate-induced strain, $\Delta\epsilon$, in Fig. 5g. The observed enhancement in T_C^* qualitatively agrees with the added tensile strain dependence symmetrically both for positive and negative V_g as shown in Fig. 5g. This indicates that the gate-induced strain has a dominant contribution to the change in the $T_C^*(V_g)$ instead of a field effect[6,7]. In the inset of Fig. 5g, we plot the experimental $\Delta T_C = T_C^*(V_g) - T_C^*(0\,V)$ versus the estimated strain $\Delta\epsilon$, together with predictions from density-functional theory calculations for 2D CGT by Li and Yang[37], considering the direct exchange interaction (solid green line), and by Dong et al.[56], attributing the enhancement of T_C to the super-exchange interaction via Cr–Te–Cr bonds (solid orange line). The closer experimental agreement with the results of Dong et al.[56] suggests that it is the decreasing energy difference between 3*d* orbitals of Cr and 5*p* orbitals of Te in nearly ~90° Cr–Te–Cr bonds of CGT that is likely to contribute to the enhancement of T_C^* as a function of strain[56]. Interestingly, we observed that the maximal T_C^* increase by mechanical strain was as much as 2.5 ± 0.6 K at $\Delta\epsilon \approx 0.026\%$. This is comparable to what was previously achieved in bulk CGT by applying an out-of-plane magnetic field of 0.7–1 T[2,8], proving that strain-based nanomechanical methods provide a compelling route for controlling and probing magneto-elastic coupling in ferromagnetic 2D layers and heterostructures.

DISCUSSION

In conclusion, we have probed the mechanical properties of CGT membranes by both static and dynamic nanomechanical means.

We demonstrated that due to CGT's strong magnetostriction[5,14] and large negative thermal expansion near T_C, bare CGT membranes experience strong resonance frequency reductions near their ferromagnetic Curie temperature and an accumulation of compressive strain. The compressive strain can produce buckling, wrinkling, or sagging of the CGT layers, which significantly complicates the analysis for nanomechanical measurements of T_C[27]. We showed that this challenge can be solved by integrating CGT in heterostructures with other materials with positive thermal expansion coefficients. This methodology can also be applied using materials that have phase transitions themselves, which we demonstrate by probing both T_N of $FePS_3$ and T_C of CGT within a single measurement of a CGT/$FePS_3$ heterostructure. The presented measurements and methodologies for nanomechanical characterization of magnetic heterostructures open up possibilities to investigate the magnetic properties that are the result of interfacial interactions in 2D magnetic heterostructures membranes[57,58], allowing also for novel magnetic properties to be discovered near the monolayer limit while excluding substrate interactions. In addition, we expect that focused studies of the mechanical dissipation in such heterostructures as a function of temperature and strain could in the future provide more insights to thermodynamics and heat transport in the 2D materials involved[27,59,60]. Finally, we showed that T_C of CGT can be enhanced by gate-induced electrostatic straining, demonstrating control of magnetic order in these ferromagnetic heterostructures using strain. We anticipate that future studies will lead to the development of membrane devices with gate-controlled magnetic actuation[61] for low-power spintronic applications.

METHODS

Device fabrication and characterization

We first pattern a diced Si/SiO_2 wafer and define circular holes with a radius of $r = 1$–2.5 μm and cavity depth of $g_0 = 285$ nm using an e-beam lithography and reactive ion etching. SiO_2 provides an electrical insulation between subsequently transferred 2D material membranes and the bottom Si electrode. To realize electrical contact to some samples for electrostatic experiments, Pd electrodes are pre-patterned on top of Si/SiO_2 chips by a lift-off technique. To create suspended membranes, thin flakes of CGT, $FePS_3$, and WSe_2 crystals are mechanically exfoliated and transferred on a pre-patterned chip by the all-dry viscoelastic stamping method[62] directly after exfoliation. Flakes of van der Waals crystals are exfoliated from high quality synthetically grown crystals with known stoichiometry. Using the same method, flakes are deterministically stacked on top of each other forming heterostructures. We stack $FePS_3$ and WSe_2 flakes on top of CGT to minimize the exposure time of the suspended CGT layers to air. Subsequently, samples are kept in an oxygen-free or vacuum environment to avoid degradation. The total time an average membrane is exposed to air during the fabrication and characterisation is in order of a few tens of minutes. No signs of degradation, such as change in optical contrast of the flakes, its thickness, or apparent disintegration of studied layers, was found during routine characterization of all samples.

Atomic force microscopy characterisation

AFM height profile scans and inspection are performed in tapping mode on a Bruker Dimension FastScan AFM. We use cantilevers with spring constants of $k_c = 30$–40 N m^{-1} for inspection. Error bars on reported thickness values are determined by measuring multiple profile scans of the same flake. For force nanoindentation experiments, we use two different cantilevers with spring constants of $k_c = 8.87 \pm 0.08$ N m^{-1} and $k_c = 18.90 \pm 0.11$ N m^{-1}. k_c for each cantilever was calibrated using thermal and solid surface deflection. We use cantilever tips with a tip radius of ~7–10 nm, as confirmed by scanning electron microscope imaging.

Laser interferometry measurements

The sample is mounted on a *xy* piezopositioning stage inside a dry optical 4 K cryostat Montana Instruments Cryostation s50. A local sample heater is used to perform temperature sweeps at a rate of ~3 K min^{-1}, keeping the pressure in the chamber below 10^{-6} mbar. A power modulated blue diode laser of $\lambda = 405$ nm is used to optothermally excite the motion of the membrane. Membrane displacement is then measured using a laser interferometer with a He–Ne laser beam of $\lambda = 632$ nm focused on the suspended membrane. In doing so, the interfering reflections from the membrane and the Si electrode underneath are recorded using a photodiode and processed by a vector network analyzer. All measurements were performed at incident laser powers of $P_{red} \leq 8$ μW and $P_{blue} \leq 1$ μW. Laser spot size is on the order of ~1 μm. During the data acquisition it is checked for all membranes that resonance frequency changes due to laser heating are insignificant. During data acquisition temperature is kept constant with ~10 mK stability by the local heater and a closed feedback loop controller. The uncertainty in measured transition temperatures is estimated from determining the peak position in $\frac{d(f_0^2)}{dT}$ within 2% accuracy in the measured maximum.

Continuum mechanics model of electrostatically strained circular membrane

A membrane suspended over a circular cavity forms a capacitor with a bottom gate electrode underneath. The change in gate voltage causes the membrane to deflect, tuning the tension and producing a shift in the resonance frequency. The resonance frequency of the fundamental vibration mode of the drum as a function of gate voltage is described as[52]:

$$f_0(V_g) = \frac{1}{2\pi}\sqrt{\frac{1}{m_{eff}}\left[\frac{2\pi E h \epsilon_0}{1-\nu^2} + \frac{8\pi E h}{(1-\nu^2)r^2}\delta_g^2 - \frac{1}{2}\frac{\partial^2 C_g}{\partial z^2}V_g^2\right]}, \quad (6)$$

where $\delta_g \approx \frac{\epsilon_0 r^2}{8 g_0^2 n(T_0)} V_g^2$ is the maximal deflection at the membrane centre[53], $\frac{\partial^2 C_g}{\partial z^2} \approx \frac{0.542 \epsilon_0 \pi r^2}{g_0^3}$ the second derivative of capacitance[53,63], and $m_{eff} = 0.27\rho h \pi r^2$ the effective mass. In the case of a heterostructure membrane, material parameters are substituted for the heterostructure analogues[29]: $E = \frac{E_1 h_1 + E_2 h_2}{h_1 + h_2}$, $\rho = \frac{\rho_1 h_1 + \rho_2 h_2}{h_1 + h_2}$, $\nu = \frac{\nu_1 h_1 + \nu_2 h_2}{h_1 + h_2}$, and $h = h_1 + h_2$. For the CGT/WSe_2 heterostructure (19.7 ± 0.1 nm/8.5 ± 0.2 nm) in Fig. 5 we use the following material parameters: $E = 89.6$ GPa, $h = 28.2$ nm, $\nu = 0.21$, $\rho = 7064$ kg m^{-3}. We extract $\epsilon = 0.079 \pm 0.004\%$, $\frac{\partial^2 C_g}{\partial z^2} = 3.46 \pm 0.11$ mFm^{-2} and $m_{eff} = 996.45$ fg from the fit in Fig. 5e, that are close to the expected values[53,63] of $\frac{\partial^2 C_g}{\partial z^2} = 2.61$ mFm^{-2} and $m_{eff} = 675.9$ fg.

DATA AVAILABILITY

The numerical data that support the findings of this study are available from the data repository. The experimental data shown in figures of the manuscript can be downloaded from the Zenodo online repository at https://doi.org/10.5281/zenodo.6501917

Received: 3 December 2021; Accepted: 13 May 2022;
Published online: 15 June 2022

REFERENCES

1. Huang, B. et al. Layer-dependent ferromagnetism in a van der Waals crystal down to the monolayer limit. *Nature* **546**, 270 (2017).
2. Gong, C. et al. Discovery of intrinsic ferromagnetism in two-dimensional van der Waals crystals. *Nature* **546**, 265 (2017).
3. Lee, J.-U. et al. Ising-type magnetic ordering in atomically thin $FePS_3$. *Nano Lett.* **16**, 7433 (2016).
4. Gibertini, M., Koperski, M., Morpurgo, A. F. & Novoselov, K. S. Magnetic 2D materials and heterostructures. *Nat. Nanotechnol.* **14**, 408 (2019).
5. Carteaux, V., Brunet, D., Ouvrard, G. & Andre, G. Crystallographic, magnetic and electronic structures of a new layered ferromagnetic compound $Cr_2Ge_2Te_6$. *J. Phys. Condens. Matter.* **7**, 69 (1995).
6. Verzhbitskiy, I. A. et al. Controlling the magnetic anisotropy in $Cr_2Ge_2Te_6$ by electrostatic gating. *Nat. Electron.* **3**, 460 (2020).
7. Wang, Z. et al. Electric-field control of magnetism in a few-layered van der Waals ferromagnetic semiconductor. *Nat. Nanotechnol.* **13**, 554 (2018).
8. Selter, S., Bastien, G., Wolter, A. U. B., Aswartham, S. & Büchner, B. Magnetic anisotropy and low-field magnetic phase diagram of the quasi-two-dimensional ferromagnet $Cr_2Ge_2Te_6$. *Phys. Rev. B* **101**, 014440 (2020).
9. Sun, Y. et al. Effects of hydrostatic pressure on spin-lattice coupling in two-dimensional ferromagnetic $Cr_2Ge_2Te_6$. *Appl. Phys. Lett.* **112**, 072409 (2018).

10. Sakurai, T. et al. Pressure control of the magnetic anisotropy of the quasi-two-dimensional van der Waals ferromagnet $Cr_2Ge_2Te_6$. *Phys. Rev. B* **103**, 024404 (2021).
11. Wang, N. et al. Transition from ferromagnetic semiconductor to ferromagnetic metal with enhanced Curie temperature in $Cr_2Ge_2Te_6$ via organic ion intercalation. *J. Am. Chem. Soc.* **141**, 17166 (2019).
12. Gupta, V. et al. Manipulation of the van der Waals magnet $Cr_2Ge_2Te_6$ by spin–orbit torques. *Nano Lett.* **20**, 7482 (2020).
13. Ostwal, V., Shen, T. & Appenzeller, J. Efficient spin-orbit torque switching of the semiconducting van der Waals ferromagnet $Cr_2Ge_2Te_6$. *Adv. Mater.* **32**, 1906021 (2020).
14. Tian, Y., Gray, M. J., Ji, H., Cava, R. J. & Burch, K. S. Magneto-elastic coupling in a potential ferromagnetic 2D atomic crystal. *2D Mater.* **3**, 025035 (2016).
15. Kozlenko, D. P. et al. Spin-induced negative thermal expansion and spin–phonon coupling in van der Waals material $CrBr_3$. *npj Quantum Mater.* **6**, 19 (2021).
16. Casto, L. D. et al. Strong spin-lattice coupling in $CrSiTe_3$. *APL Mater.* **3**, 041515 (2015).
17. McGuire, M. A., Dixit, H., Cooper, V. R. & Sales, B. C. Coupling of crystal structure and magnetism in the layered, ferromagnetic insulator CrI_3. *Chem. Mater.* **27**, 612–620 (2015).
18. Schneeloch, J. A. et al. Gapless Dirac magnons in $CrCl_3$. Preprint at https://arxiv.org/abs/2110.10771v1 (2021).
19. Miao, F., Liang, S.-J. & Cheng, B. Straintronics with van der Waals materials. *npj Quantum Mater.* **6**, 59 (2021).
20. Yang, S., Chen, Y. & Jiang, C. Strain engineering of two-dimensional materials: Methods, properties, and applications. *InfoMat* **3**, 397–420 (2021).
21. Chen, C. et al. Performance of monolayer graphene nanomechanical resonators with electrical readout. *Nat. Nanotechnol.* **4**, 861 (2009).
22. Zhang, X. et al. Dynamically-enhanced strain in atomically thin resonators. *Nat. Commun.* **11**, 5526 (2020).
23. Lee, C., Wei, X., Kysar, J. W. & Hone, J. Measurement of the elastic properties and intrinsic strength of monolayer graphene. *Science* **321**, 5887 (2008).
24. Chen, C. et al. Graphene mechanical oscillators with tunable frequency. *Nat. Nanotechnol.* **8**, 923 (2013).
25. Lemme, M. C. et al. Nanoelectromechanical sensors based on suspended 2D materials. *Research* **2020**, 8748602 (2020).
26. Steeneken, P. G., Dolleman, R. J., Davidovikj, D., Alijani, F. & van der Zant, H. S. J. Dynamics of 2D material membranes. *2D Mater.* **8**, 042001 (2021).
27. Šiškins, M. et al. Magnetic and electronic phase transitions probed by nanomechanical resonators. *Nat. Commun.* **11**, 2698 (2020).
28. Morell, N. et al. High quality factor mechanical resonators based on WSe_2 monolayers. *Nano Lett.* **16**, 5102 (2016).
29. Ye, F., Lee, J. & Feng, P. X.-L. Atomic layer MoS_2-graphene van der Waals heterostructure nanomechanical resonators. *Nanoscale* **9**, 18208 (2017).
30. Jiang, S., Xie, H., Shan, J. & Mak, K. F. Exchange magnetostriction in two-dimensional antiferromagnets. *Nat. Mater.* **19**, 1295 (2020).
31. Ni, Z. et al. Imaging the Néel vector switching in the monolayer antiferromagnet $MnPSe_3$ with strain-controlled Ising order. *Nat. Nanotechnol.* **16**, 782–787 (2021).
32. Liu, K. et al. Elastic properties of chemical-vapor-deposited monolayer MoS_2, WS_2, and their bilayer heterostructures. *Nano Lett.* **14**, 5097 (2014).
33. Kim, S., Yu, J. & van der Zande, A. M. Nano-electromechanical drumhead resonators from two-dimensional material bimorphs. *Nano Lett.* **18**, 6686 (2018).
34. Novoselov, K. S., Mishchenko, A., Carvalho, A. & Neto, A. H. C. 2D materials and van der Waals heterostructures. *Science* **353**, aac9439 (2016).
35. Castellanos-Gomez, A. et al. Elastic properties of freely suspended MoS_2 nanosheets. *Adv. Mater.* **24**, 772 (2012).
36. de Jong, M. et al. Charting the complete elastic properties of inorganic crystalline compounds. *Sci. Data* **2**, 150009 (2015).
37. Li, X. & Yang, J. $CrXTe_3$ (X = Si, Ge) nanosheets: Two dimensional intrinsic ferromagnetic semiconductors. *J. Mater. Chem. C* **2**, 7071 (2014).
38. Cantos-Prieto, F. et al. Layer-dependent mechanical properties and enhanced plasticity in the van der Waals chromium trihalide magnets. *Nano Lett.* **21**, 3379–3385 (2021).
39. Castellanos-Gomez, A. et al. Single-layer MoS_2 mechanical resonators. *Adv. Mater.* **25**, 6719 (2013).
40. Lyon, K. G., Salinger, G. L., Swenson, C. A. & White, G. K. Linear thermal expansion measurements on silicon from 6 to 340 K. *J. Appl. Phys.* **48**, 865 (1977).
41. Chen, T., Pauly, M. & Reis, P. M. A reprogrammable mechanical metamaterial with stable memory. *Nature* **589**, 386 (2021).
42. Mahboob, I. & Yamaguchi, H. Bit storage and bit flip operations in an electromechanical oscillator. *Nat. Nanotechnol.* **3**, 275 (2008).
43. Roodenburg, D., Spronck, J. W., van der Zant, H. S. J. & Venstra, W. J. Buckling beam micromechanical memory with on-chip readout. *Appl. Phys. Lett.* **94**, 183501 (2009).
44. Zhang, R., Koutsos, V. & Cheung, R. Elastic properties of suspended multilayer WSe_2. *Appl. Phys. Lett.* **108**, 042104 (2016).
45. Çakír, D., Peeters, F. M. & Sevik, C. Mechanical and thermal properties of h-MX_2 (M = Cr, Mo, W; X = O, S, Se, Te) monolayers: A comparative study. *Appl. Phys. Lett.* **104**, 203110 (2014).
46. Lifshitz, R. & Roukes, M. L. Thermoelastic damping in micro- and nanomechanical systems. *Phys. Rev. B* **61**, 5600 (2000).
47. Sun, Y., Fang, D. & Soh, A. K. Thermoelastic damping in micro-beam resonators. *Int. J. Solids. Struct.* **43**, 3213 (2006).
48. Agarwal, M. & Wani, P. Growth conditions and crystal structure parameters of layer compounds in the series $Mo_{1-x}W_xSe_2$. *Mater. Res. Bull.* **14**, 825 (1979).
49. Zeng, F., Zhang, W.-B. & Tang, B.-Y. Electronic structures and elastic properties of monolayer and bilayer transition metal dichalcogenides MX_2 (M = Mo, W; X = O, S, Se, Te): A comparative first-principles study. *Chinese Phys. B* **24**, 097103 (2015).
50. Khan, S. et al. Spin dynamics study in layered van der Waals single-crystal $Cr_2Ge_2Te_6$. *Phys. Rev. B* **100**, 134437 (2019).
51. Hashemi, A., Komsa, H.-P., Puska, M. & Krasheninnikov, A. V. Vibrational properties of metal phosphorus trichalcogenides from first-principles calculations. *J. Phys. Chem. C* **121**, 27207 (2017).
52. Chen, C. *Graphene nanoelectromechanical resonators and oscillators* (PhD thesis, Columbia University, 2013).
53. Weber, P., Güttinger, J., Tsioutsios, I., Chang, D. E. & Bachtold, A. Coupling graphene mechanical resonators to superconducting microwave cavities. *Nano Lett.* **14**, 2854 (2014).
54. Wunnicke, O. Analytical model of the quasistatic mechanical behavior of galvanic piezoelectric microelectromechanical system switches. *J. Appl. Phys.* **106**, 104502 (2009).
55. Roldán, R., Castellanos-Gomez, A., Cappelluti, E. & Guinea, F. Strain engineering in semiconducting two-dimensional crystals. *J. Phys.: Condens. Matter* **27**, 313201 (2015).
56. Dong, X.-J., You, J.-Y., Zhang, Z., Gu, B. & Su, G. Great enhancement of Curie temperature and magnetic anisotropy in two-dimensional van der Waals magnetic semiconductor heterostructures. *Phys. Rev. B* **102**, 144443 (2020).
57. Zhang, L. et al. Proximity-coupling-induced significant enhancement of coercive field and Curie temperature in 2D van der Waals heterostructures. *Adv. Mater.* **32**, 2002032 (2020).
58. Wang, Y. et al. Modulation doping via a two-dimensional atomic crystalline acceptor. *Nano Lett.* **20**, 8446–8452 (2020).
59. Dolleman, R. J. et al. Optomechanics for thermal characterization of suspended graphene. *Phys. Rev. B* **96**, 165421 (2017).
60. Morell, N. et al. Optomechanical measurement of thermal transport in two-dimensional $MoSe_2$ lattices. *Nano Lett.* **19**, 3143 (2019).
61. Ben-Shimon, Y. & Ya'akobovitz, A. Magnetic excitation and dissipation of multilayer two-dimensional resonators. *Appl. Phys. Lett.* **118**, 063103 (2021).
62. Castellanos-Gomez, A. et al. Deterministic transfer of two-dimensional materials by all-dry viscoelastic stamping. *2D Mater.* **1**, 011002 (2014).
63. Will, M. et al. High quality factor graphene-based two-dimensional heterostructure mechanical resonator. *Nano Lett.* **17**, 5950 (2017).

ACKNOWLEDGEMENTS

The authors thank B. Simon for continuous support and feedback on the manuscript. M.Š., M.L., H.S.J.v.d.Z., and P.G.S. acknowledge funding from the European Union's Horizon 2020 research and innovation programme under grant agreement number 881603. H.S.J.v.d.Z., E.C., and S.M.-V. thank COST Action MOLSPIN CA15128; E.C. and S.M.-V. acknowledge the financial support from the European Union (ERC AdG Mol-2D 788222), the Spanish MICINN (MAT2017-89993-R co-financed by FEDER and Excellence Unit "María de Maeztu", CEX2019-000919-M) and the Generalitat Valenciana (Prometeo programme and PO FEDER Programme, ref. IDIFEDER/2018/061 and IDIFEDER/2020/063). W.X., S.J., and W.H. thank National Natural Science Foundation of China (11974025). S.K. and T.v.d.S. acknowledge financial support by the Dutch Research Council (NWO Projectruimte grant 680.91.115).

AUTHOR CONTRIBUTIONS

M.Š., S.K., E.C., H.S.J.v.d.Z., T.v.d.S., and P.G.S. conceived the experiments. M.Š. performed the laser interferometry measurements. M.Š. and M.L. fabricated and inspected the samples. S.M.-V. and E.C. synthesized and characterized the $FePS_3$ crystals. W.X., S.J., and W.H. synthesized and characterized the $Cr_2Ge_2Te_6$ crystals. M.Š., S.K., and B.J.M.S. analyzed and modelled the experimental data. H.S.J.v.d.Z., T.v.d.S., and P.G.S. supervised the project. The paper was jointly written by all authors with a main contribution from M.Š. All authors discussed the results and commented on the paper.

COMPETING INTERESTS

The authors declare no competing interests.

ADDITIONAL INFORMATION

Supplementary information The online version contains supplementary material available at https://doi.org/10.1038/s41699-022-00315-7.

Correspondence and requests for materials should be addressed to Makars. Šiškins, Toenovander Sar, Herre S. J.vander Zant or Peter G. Steeneken.